Supporting materials for

Warm-Sector Heavy Rainfall over the Eastern China Plains: Identification, Characteristics, and Precursor Dynamic Signals

Weilong Deng [a, b], Jianping Guo [b, e, *], Ning Li [b, c], Zhen Zhang [b, d], Yifei Wang [b], Yi Yang [a, *]

[a] *College of Atmospheric Sciences, Lanzhou University, Lanzhou 730000, China*

[b] *State Key Laboratory of Severe Weather Meteorological Science and Technology & Specialized Meteorological Support Technology Research Center, Chinese Academy of Meteorological Sciences, China Meteorological Administration, Beijing 100081, China*

[c] *College of Earth and Planetary Sciences, University of Chinese Academy of Sciences, Beijing 100049, China*

[d] *Department of Atmospheric and Oceanic Sciences & Institute of Atmospheric Sciences, Fudan University, Shanghai 200438, China*

[e] *CMA Field Scientific Experiment Base for Low-Altitude Economy Meteorological Support of Unmanned Aviation in Guangdong-Hong Kong-Macao Greater Bay Area, Shenzhen 518108, China*

Correspondence to:

Dr./Prof. Jianping Guo (Email: jpguocams@gmail.com) and Dr./Prof. Yi Yang (Email: yangyi@lzu.edu.cn)

1. Objective frontal detection based on the Thermal Front Parameter

Following the framework of Renard and Clarke (1965), Hewson (1998) and Jenkner et al. (2010), and adapted to the warm-season North China configuration of Fu et al. (2020), an automated front-detection algorithm was developed and applied to ERA5 hourly reanalysis on the 850-hPa isobaric surface over the domain 97°–132°E, 22°–57°N (14640 hourly time steps spanning the analysis period). The algorithm comprises three modules that

(i) compute diagnostic fields from the 850-hPa pseudo-equivalent potential temperature (θ_e),

(ii) apply masking and threshold rules to retain candidate fronts, and

(iii) invert the retained fronts for type, length, and position.

A flow chart of the procedure is given in Fig. S1, and a worked example for 1700 BJT, August 18, 2023 is shown in Fig. S2.

1.1. Input data and pre-processing

For each hourly time step T_i, the specific humidity q, relative humidity RH, air temperature T, and the horizontal wind components u and v at 850 hPa were extracted from ERA5 (0.25° × 0.25°). The pseudo-equivalent potential temperature θ_e was computed from T, q and pressure following Bolton (1980). To suppress the high-frequency noise to which the second- and third-order spatial derivatives of θ_e are extremely sensitive, the θ_e field was smoothed eight times with a Gaussian filter, consistent with Jenkner et al. (2010) and Fu et al. (2020).

1.2. Diagnostic fields (Module i)

Four diagnostic fields are then derived on the smoothed θ_e field. The Thermal Front Parameter (TFP; Renard and Clarke, 1965; Hewson, 1998) is defined as the projection of the gradient of the gradient magnitude of θ_e onto the unit vector pointing down-gradient:

$$\mathrm{TFP} = -\nabla|\nabla\theta_e| \cdot \frac{\nabla\theta_e}{|\nabla\theta_e|} \qquad (S1)$$

In addition, the gradient magnitude of θ_e (used as a measure of frontal strength), the masking parameter MP, and the front-normal wind component V_f are computed as:

$$\mathrm{GEPT} = |\nabla\theta_e| \tag{S2}$$

$$\mathrm{MP} = -\frac{\nabla\theta_e \cdot \nabla|\nabla\theta_e|}{|\nabla\theta_e|} \tag{S3}$$

$$V_f = \mathbf{V}_{850} \cdot \frac{\nabla\theta_e}{|\nabla\theta_e|} \tag{S4}$$

where $\mathbf{V}_{850} = (u, v)$ is the 850-hPa horizontal wind, and $\frac{\nabla\theta_e}{|\nabla\theta_e|}$ is the unit vector along $\nabla\theta_e$, which by construction points from the cold air toward the warm air. Hence positive (negative) V_f indicates motion of the front toward (away from) the warm air, i.e., cold-frontal (warm-frontal) propagation. All horizontal derivatives were evaluated by centered differences on the spherical grid, and TFP and MP were converted to units of K (100 km)$^{-2}$ for visualization.

The locus $\mathrm{TFP} = 0$ identifies the line along which $|\nabla\theta_e|$ is maximized in the down-gradient direction, i.e., the center of the frontal zone (Hewson, 1998).

1.3. Masking and threshold rules (Module ii)

Three successive rules are applied to convert raw $\mathrm{TFP} = 0$ contours into synoptic-scale fronts.

Rule A — Strength and warm-side masking. Only grid points satisfying both

$$\mathrm{GEPT} \geq K_1 = 4\ \mathrm{K}\,(100\ \mathrm{km})^{-1}\ \&\ \mathrm{MP} \leq 0 \tag{S5}$$

are retained. The first criterion isolates strongly baroclinic zones, while $\mathrm{MP} \leq 0$ restricts the candidate to the warm side of the frontal zone, which in the Hewson (1998) framework corresponds to the operationally drawn front line. The threshold $K_1 = 4\ \mathrm{K}\,(100\ \mathrm{km})^{-1}$ was selected for warm-season North China and is consistent with the value adopted by Fu et al. (2020) and Song et al. (2023).

Rule B — Extraction of $\mathrm{TFP} = 0$ contour segments. Within the binary mask defined by Eq. (S5), zero-contours of TFP are extracted using the marching-squares algorithm. Each connected polyline constitutes a candidate front.

Rule C — Synoptic length filter. The arc length of each candidate front is measured along its polyline. Candidates shorter than 10° of arc are discarded as sub-synoptic noise, and the remainder are promoted to synoptic fronts.

1.4. Front-type, length and position inversion (Module iii)

For each retained synoptic front, three attributes are diagnosed.

Position. The geometric position of the front is given by the sequence of vertices $\{(\lambda_k, \varphi_k)\}$, k = 1, 2, …, N, that define the $\mathrm{TFP} = 0$ polyline, where λ_k and φ_k are the longitude and latitude of the k-th vertex along the polyline. As shown by Hewson (1998), this locus coincides with the center of the baroclinic zone.

Length. The arc length is reported in both degrees and kilometers.

Type. The polyline is resampled into M equispaced points and the front-normal wind $V_{f,m}$ is interpolated from the 850-hPa u and v fields at each sampling point using bilinear interpolation. The along-front mean

$$\bar{V_f} = \frac{1}{M}\sum_{m=1}^{M} V_{f,m} \qquad (S6)$$

is converted to m s^{-1} and used to classify the front following Berry et al. (2011) and the rules in Fu et al. (2020):

$$\text{Front type} = \begin{cases} \text{Quasi-stationary front,} & |\bar{V_f}| \leq 1.5\ \mathrm{m\,s^{-1}}, \\ \text{Cold front,} & \bar{V_f} > +1.5\ \mathrm{m\,s^{-1}}, \\ \text{Warm front,} & \bar{V_f} < -1.5\ \mathrm{m\,s^{-1}}. \end{cases} \qquad (S7)$$

The classified fronts at T_i are written to the synoptic frontal field $\mathrm{SFF}[T_i]$, together with their geometric coordinates, length, $\bar{V_f}$, and type label.

1.5. Worked example: 1700 BJT, August 18, 2023

Figure S2 illustrates the algorithm at 1700 BJT, August 18, 2023. Panel (a) shows the smoothed 850-hPa θ_e field overlaid with the 850-hPa wind. The navy polygon outlines the warm, moist air mass (340–344 K) over the North China Plain. A sharp θ_e gradient marks its northern and northwestern edge (35–40°N), where northerly flow advects cooler air. Panel (b) shows the TFP field with the contours $\mathrm{TFP} = 0$ (green), $\mathrm{GEPT} = 4\mathrm{K}$ (100 km)$^{-1}$ (black) and $\nabla^2|\mathrm{GEPT}| = 0$ (yellow). Segments satisfying Rules A–C (blue) are the candidate fronts. The principal segment crosses the analysis box (104.5–129.5°E, 24.5–46.5°N), exceeds 10° in arc length, and is classified as a cold front.

2. Identification of Low-level jet

An LLJ is identified from each 6-min RWP profile as a low-level wind-speed maximum (a jet nose) overlain by substantial shear. Its strength is the wind-speed maximum at the nose, V_{max}. The shear parameter is $\Delta V = V_{max} - V_{min}$, where V_{min} is the first wind-speed minimum above the core; when no minimum is found below 3 km, the speed at 3 km (V_{3km}) is used, so that $\Delta V = V_{max} - V_{3km}$. Following Whiteman et al. (1997), a profile is taken to contain an LLJ when $V_{max} > 10$ m s^{-1} within the lowest 3 km AGL and $\Delta V \geq 5$ m s^{-1}. The height and direction of the LLJ are those of V_{max}. A worked example, showing the jet core, the wind-speed minimum above it, and the resulting ΔV, is given in Fig. S3.

When a profile shows more than one jet nose, as in the double-nosed or double low-level jet structures in which a boundary-layer jet underlies a synoptic-system-related jet (Du and Chen, 2018, 2019), only the strongest nose (the largest V_{max}) is retained, and the two jets are not identified or treated separately. This single-maximum treatment follows the classical jet-core criterion of Bonner (1968) and Whiteman et al. (1997).

3. Bootstrap confidence intervals for the LLJ occurrence frequency

The statistical robustness of the LLJ occurrence frequency (Fig. 11c) was assessed with an event-level bootstrap procedure. The 62 WSHR events were resampled with replacement 1000 times. For each resampled set, the occurrence frequency was recomputed at every 6-min step over the 180 min preceding the onset of rainfall. At each time step, the 2.5th and 97.5th percentiles of the resampled frequencies define the

95% confidence interval shown as shading in Fig. 11c. Entire events, rather than individual profiles, were resampled, so that the temporal correlation within each event is preserved.

The rise in occurrence frequency toward the onset of rainfall was further tested with a paired comparison. For each event, the occurrence proportion of the LLJ in the final 60 min was compared with that in the first 60 min of the window (−180 to −120 min). The mean paired difference is 7.0 percentage points, with a bootstrap 95% confidence interval of 0.1 to 14.1 percentage points (1000 iterations). The interval excludes zero, indicating a statistically robust increase.

References

Berry, G., Reeder, M. J., and Jakob, C.: A global climatology of atmospheric fronts, Geophys. Res. Lett., 38, L04809, https://doi.org/10.1029/2010GL046451, 2011.

Bolton, D.: The computation of equivalent potential temperature, Mon. Weather Rev., 108, 1046–1053, https://doi.org/10.1175/1520-0493(1980)108<1046:TCOEPT>2.0.CO;2, 1980.

Bonner, W. D.: Climatology of the low level jet, Mon. Weather Rev., 96, 833–850, https://doi.org/10.1175/1520-0493(1968)096<0833:COTLLJ>2.0.CO;2, 1968.

Du, Y. and Chen, G.: Heavy rainfall associated with double low-level jets over Southern China. Part I: Ensemble-based analysis, Mon. Weather Rev., 146, 3827–3844, https://doi.org/10.1175/MWR-D-18-0101.1, 2018.

Du, Y. and Chen, G.: Heavy rainfall associated with double low-level jets over Southern China. Part II: Convection initiation, Mon. Weather Rev., 147, 543–565, https://doi.org/10.1175/MWR-D-18-0102.1, 2019.

Fu, J., Zhang, F., and Hewson, T. D.: Object-Oriented Composite Analysis of Warm-Sector Rainfall in North China, Mon. Weather Rev., 148, 2719–2735, https://doi.org/10.1175/MWR-D-19-0038.1, 2020.

Hewson, T. D.: Objective fronts, Meteorol. Appl., 5, 37–65, https://doi.org/10.1017/S1350482798000553, 1998.

Jenkner, J., Sprenger, M., Schwenk, I., Schwierz, C., Dierer, S., and Leuenberger, D.: Detection and climatology of fronts in a high-resolution model reanalysis over the Alps, Meteorol. Appl., 17, 1–18, https://doi.org/10.1002/met.142, 2010.

Renard, R. J. and Clarke, L. C.: Experiments in numerical objective frontal analysis, Mon. Weather Rev., 93, 547–556, https://doi.org/10.1175/1520-0493(1965)093<0547:EINOFA>2.3.CO;2, 1965.

Whiteman, C. D., Bian, X., and Zhong, S.: Low-level jet climatology from enhanced rawinsonde observations at a site in the southern Great Plains, J. Appl. Meteorol., 36, 1363–1376, https://doi.org/10.1175/1520-0450(1997)036<1363:LLJCFE>2.0.CO;2, 1997.

Figures

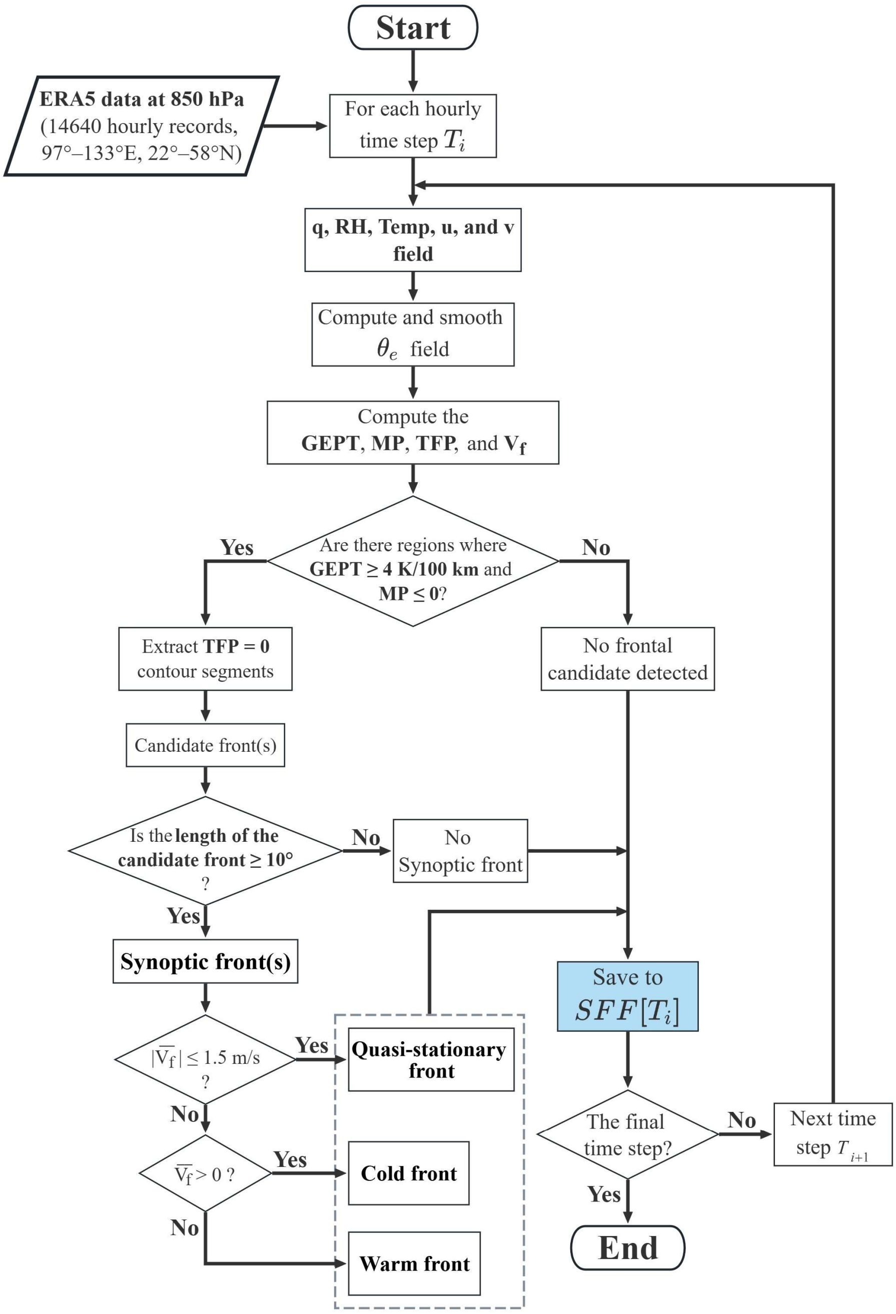

Figure S1. Flow chart of the objective front-detection algorithm (Sect. 1) applied to the hourly 850-hPa ERA5 fields. GEPT denotes the magnitude of the θ_e gradient, MP the masking parameter, TFP the thermal front parameter, and V_f the along-front mean front-normal wind. Fronts retained at each time step T_i are written to the synoptic frontal field $SFF[T_i]$.

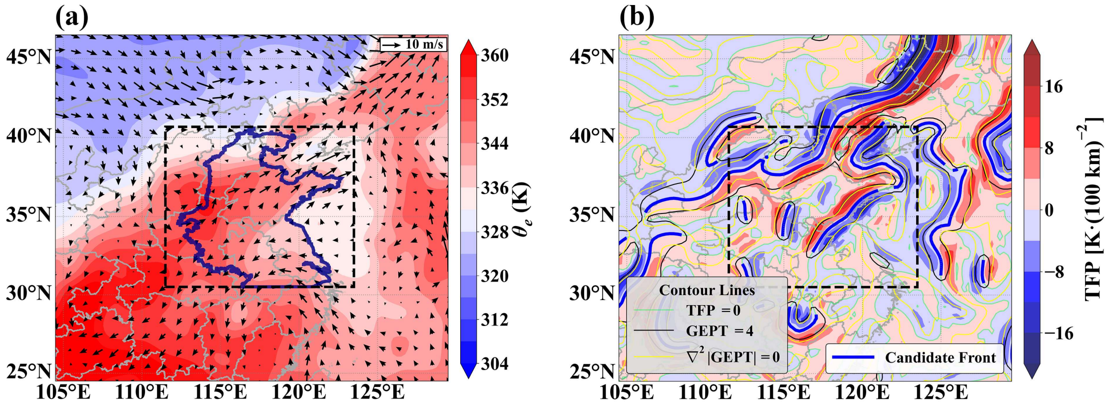

Figure S2. Worked example of the front-detection algorithm at 1700 BJT, August 18, 2023 (Sect. 1.5). (a) Smoothed 850-hPa θ_e (shading; K) and 850-hPa wind (vectors); the navy polygon outlines the warm, moist air mass (340–344 K). (b) TFP [shading; K (100 km)$^{-2}$] with the TFP = 0 (green), GEPT = 4 K (100 km)$^{-1}$ (black), and ∇^2|GEPT| = 0 (yellow) contours; candidate fronts satisfying Rules A–C are drawn in blue.

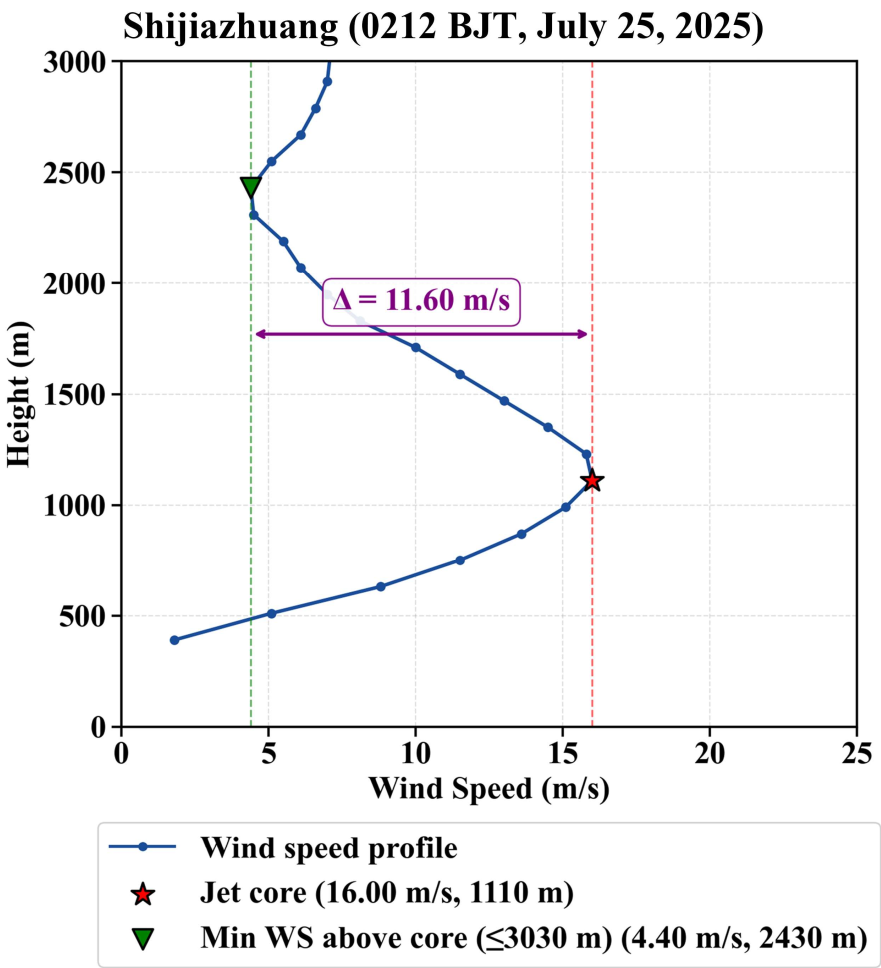

Figure S3. Worked example of the low-level jet (LLJ) identification (Sect. 2) for Shijiazhuang station at 0212 BJT, July 25, 2025. The wind-speed profile (blue) has its jet core (red star) at V_{max} = 16.0 m s^{-1} and 1110 m AGL; the wind-speed minimum above the core (green triangle) is 4.4 m s^{-1} at 2430 m, giving ΔV = 11.6 m s^{-1}. Both criteria ($V_{max} \geqslant$ 10 m s^{-1} and $\Delta V \geq 5$ m s^{-1}) are satisfied.